Structural changes and viscoplastic behavior of a generic embedded-atom model metal in steady shear flow

Igor Stankovic* and Siegfried Hess

Institut für Theoretische Physik, PN 7-1, Fakultät II, Technische Universität Berlin, D-10623 Berlin, Germany

Martin Kröger

Polymer Physics, Materials Science, ETH Zürich, CH-8092 Zürich, Switzerland

We study equilibrium and nonequilibrium properties of a simple ''generic embedded-atom model'' (GEAM) for metals. The model allows to derive simple analytical expressions for several zero-temperature constitutive properties—in overall agreement with real metals. The model metal is then subjected to shear deformation and strong flow via nonequilibrium molecular dynamics simulation in order to discuss the origins of some qualitative properties observed using more specific embedded-atom potentials. The ''common neighbor analysis,'' based on planar graphs is used to obtain information about the transient structures accompanying viscoplastic behavior on an atomic level. In particular, pressure tensor components and plastic yield are investigated and correlated with underlying structural changes. A simple analytical expression for the isotropic pressure at finite temperatures is proposed. A nonequilibrium phase diagram is obtained by semianalytic calculation.

I. INTRODUCTION

An understanding of the processes accompanying plastic deformation of solids is of fundamental interest to material science. Crystalline materials and metals, in particular, deform when subjected to stress. After reaching a maximum (yield) stress, the material does not return to its original shape when relieving external forces. The extent of structural change depends on the magnitude and rate of deformation. For small and slow deformations cooperative motions of atoms—and the displacement of full layers—are observed. Irreversible plastic deformation at low shear rates is usually described through the motion of microscopic defects, such as dislocations, voids, microcracks, and grain boundaries [1–5]. When subjected to steady shear, however, the system undergoes significant structural transformations on a range of length scales, as known from atomic force microscopy (AFM). Tribology has approached the microscopic level [6–10], but AFM does not operate at the high speeds needed to investigate a strong flow regime which will be also investigated in this work. Along with its bulk properties, metals reveal still incompletely resolved surface phenomena, e.g., during dry solid friction, wear, and abrasion [11–13]. Dry solid friction of two metal bodies involves the formation, growth, and disappearance of a number of small contact zones (asperities, area typically of the order of 10 μm^2 while occupying 0.1% of the visible area), in which friction forces are thought to build up [14–16]. Low energy electron diffraction experiments proved the existence of crystal structures at the sliding surfaces that are aligned with the shear direction in abraded material [17]. The observed structural changes, originated by large relative speeds in the surface layers—at a moderate overall speed—may propagate over several thousand crystal lattice constants [11–13,17]. Thus, the frictional force—the shear stress integrated over the volume of the asperities—must be considered as inhomogeneous with respect to density, velocity, and temperature fields. An understanding of the physical mechanisms in the mentioned strong nonequilibrium situations is relevant for several phenomena including the processes inside the earth's crust [18], high velocity deformations, and breaking of metals at high velocities and impacts [19,20].

In this work, we adopt the embedded-atom method [20–23] to model metals and to investigate microscopic origins of the observed macroscopic behavior. This method takes into account that energy of atoms in metals depends on local electron density, resulting in forces that are many body in character. Simulation provides us with the time-dependent positions and momenta of atoms in the system and thus allows for a detailed structure-relationship analysis (for example, by using planar graphics [24]). A particularly simple choice of model, the ''generic embedded-atom model'' (GEAM), will be shown to reproduce the main zero-temperature constitutive properties of real metal by varying a set of basic model parameters. It is characterized by a few model parameters, the strength of the embedding function, the position of the minimum, and the cutoff radius of an interatomic binary potential, thus allowing for a systematic analysis of the influence of constitutive properties on the structure and mechanical behavior of metals. The parameters independently adjust several constitutive properties (elastic coefficients, vacancy formation, and cohesive energy) such that we can adjust them through analyzing corresponding properties of real metals. In particular, only the ''quadratic term'' in the embedding functional contributes to the elastic coefficients, which include response to volume changing deformation (bulk modulus B, C_{11}, and C_{12}) since they depend on the second derivative of the cohesive energy. We simulate shear flow of the model metal within a single asperity, at a

---

*Corresponding author. Email address: stankovic@itp.physik.tu-berlin.de

length scale where local properties, e.g., temperature and density of the macroscopic body can be considered gradient-free. For the case of sliding friction we simulate a contact zone at a relative motion in x direction, with a load and shear gradient in y direction. The value of penetration hardness is a good estimate for the typical pressure in the contact area, for the case of rough surfaces and moderate loads [14]. Recent work [25–27] on friction between a rolling wheel and a rail combines plastic deformation, friction, and heat generation effects with Hertzian calculations of stress distribution. The study reveals information about the feedback effects of temperature on shear stress and shear on structure, neither of which are included in the aforementioned work on rolling friction. The simulation allows to measure the influence of initial crystal orientation on transient flow behaviors, the formation of shear bands and dislocations, and the general rate dependence of metal flow behavior in its viscoplastic (strong) flow regime. We present semianalytic calculations of the nonequilibrium phase diagram, structure, and shear stress of the systems with fcc, bcc, and fluid (molten state) stationary configurations. Special attention is paid to the effect of temperature on the structural behavior. Further, we describe the evolution of isotropic pressure, as well as bulk and shear moduli with temperature for different densities. A simple approximate expression for isotropic pressure will be obtained.

Two recently developed grid-free computer simulation techniques, smooth particle applied mechanics [28–30] and dissipative particle dynamics [31], offer the potential for modeling metals on a micrometer scale ("mesoscale"). These methods allow us to study the impacts, high velocity deformations, formation of contact zones, and processes inside contact zones during dry friction of two metal blocks. However, they rely on expressions for thermomechanical properties of model metals as input. One of the goals of this work is to provide these expressions based on a generic, yet *ab initio* motivated model.

This paper is organized as follows: in Sec. II A we introduce the embedded-atom method and present expressions for the pressure and elastic modulus tensors. In Sec. III the model, its format, some of its static properties, and reference values are given. Implementation details are discussed in Sec. III C. The remaining sections analyze the elastic behavior (Sec. IV), the mechanical behavior of a shear flow simulation (Sec. V), and the nonequilibrium structure of the model metal (Sec. VI) subjected to steady shear.

II. THE EMBEDDED-ATOM METHOD

We consider a model metal composed of N atoms at thermal equilibrium at temperature T located at positions $\mathbf{r}^i$, $i = 1, 2, \ldots, N$ contained in a volume V. The potential is the sum of two contributions to the total potential energy E: a conventional binary interaction term through a two-body interaction potential $\mathcal{U}$ and a term stemming from an embedding functional $\mathcal{F}$, which models the effect of the electronic "glue" between atoms [21,22]:

$$E = \sum_{i=1}^{N} \left[\mathcal{F}(\rho_i) + \sum_{j>i}^{N} \mathcal{U}(r^{ij}) \right], \qquad (1)$$

where r^{ij} denotes the norm of the relative vector $\mathbf{r}^{ij} = \mathbf{r}_i - \mathbf{r}_j$ between atoms i and j. The embedding functional $\mathcal{F}$ has to be a nonlinear function of the (local) embedding densities ρ_i of atoms $i = 1, \ldots, N$. The local embedding density ρ_i is constructed from the radial coordinates of surrounding atoms and requires the choice of a weighting function $w(r)$,

$$\rho_i = \sum_{j \neq i} w(r^{ij}) + w(0). \qquad (2)$$

Here, $w(0)$ is the local embedding density of a solitary atom. The (effectively many-body) model potentials introduced above serve to model a variety of metal properties. The potential contributions to the pressure tensor and the elastic moduli can be obtained from the terms of first and second order in the expansion of the configurational free energy with respect to the Lagrangian strain tensor $s_{\mu\nu}$, defined through particle displacement written as $r_\nu^i \rightarrow r_\nu^i + r_\mu^i s_{\mu\nu}$. The Greek subscripts μ, ν stand for Cartesian components associated with the x, y, z directions. This expansion is obtained from the standard expression for the configurational Helmholtz free energy $\beta F^{\text{pot}} = -\ln \int \exp(-\beta E) \, d\mathbf{r}^N$ with $\beta \equiv 1/(k_B T)$.

Pressure and elastic modulus tensors

The total pressure tensor is a sum of kinetic and potential contributions. The potential part of the pressure is evaluated as a N-particle average according to [32]

$$V p_{\mu\nu}^{\text{pot}} = \langle \Phi_{\mu\nu} \rangle, \quad \Phi_{\mu\nu} = \sum_{i \neq j} \phi_{\mu\nu}^i(r^{ij}). \qquad (3)$$

The symbol $\Sigma_{i \neq j}$ denotes a double summation over pairs ij of (different) particles, the angular brackets indicate an ensemble or time average, and the second rank tensor ϕ^i ($i \in 1, \ldots, N$) is given by

$$\phi_{\mu\nu}^i(r^{ij}) = r_\mu^{ij} \left(\frac{1}{2} \boldsymbol{\nabla}_\nu \mathcal{U}(r^{ij}) + \left. \frac{\partial \mathcal{F}(\rho)}{\partial \rho} \right|_i \boldsymbol{\nabla}_\nu w(r^{ij}) \right), \qquad (4)$$

where $\boldsymbol{\nabla}_\nu w(\mathbf{r}) = r^{-1} r_\nu \, \partial w(r)/\partial r$ as for any function with spherical symmetry, i.e., when $w(\mathbf{r}) = w(r)$.

The kinetic part of the pressure p^{kin} is obtained from peculiar velocity of particles, $\mathbf{c}^i = \dot{\mathbf{r}}^i - \mathbf{v}(\mathbf{r}^i)$, where $\mathbf{v}(\mathbf{r}^i)$ denotes the (macroscopic) flow velocity on position of particle i,

$$V p_{\mu\nu}^{\text{kin}} = \left\langle \sum_i m c_\mu^i c_\nu^i \right\rangle. \qquad (5)$$

The scalar (isotropic) pressure p^{iso} is the trace of the total pressure tensor divided by the spatial dimension, $p^{\text{iso}} = p_{\mu\mu}/3$. The symmetric traceless part of $p_{\mu\nu}$ is associated with the shear stress and normal stress differences. The antisymmetric part of the pressure tensor vanishes for structureless particles with spherical interaction.

The response of the material to deformation $s_{\mu\nu}$ is characterized by the elastic modulus tensor $G_{\lambda\kappa,\mu\nu}$, defined by

linear relation $\sigma_{\lambda\kappa} = G_{\lambda\kappa,\mu\nu} s_{\mu\nu}$, where $\sigma_{\lambda\kappa} = -(p_{\lambda\kappa}^{\mathrm{pot,def}} - p_{\lambda\kappa}^{\mathrm{pot,0}})$ is the negative difference between the potential contribution to the pressure tensor in the deformed state $p_{\lambda\kappa}^{\mathrm{pot,def}}$ and its corresponding value $p_{\lambda\kappa}^{\mathrm{pot,0}}$ in the undeformed state. The elastic modulus tensor can be decomposed into Born-Green and fluctuation contributions, $G_{\lambda\kappa,\mu\nu} = G_{\lambda\kappa,\mu\nu}^{\mathrm{BG}} + G_{\lambda\kappa,\mu\nu}^{\mathrm{flct}}$ [32,33], with

$$VG_{\lambda\kappa,\mu\nu}^{\mathrm{BG}} = \left\langle \sum_{i \neq j} \phi_{\lambda\kappa,\mu\nu}^i(\mathbf{r}^{ij}) \right\rangle_0 + \frac{1}{3}\langle \Phi_{\mu\mu}\rangle_0 \delta_{\lambda\kappa}\delta_{\mu\nu}, \quad (6)$$

$$VG_{\lambda\kappa,\mu\nu}^{\mathrm{flct}} = -\beta[\langle \Phi_{\lambda\kappa}\Phi_{\mu\nu}\rangle_0 - \langle \Phi_{\lambda\kappa}\rangle_0\langle \Phi_{\mu\nu}\rangle_0]. \quad (7)$$

In Eq. (6) we use the abbreviation $\phi_{\lambda\kappa,\mu\nu}^i(\mathbf{r}) = r_\lambda \nabla_\kappa \phi_{\mu\nu}^i(\mathbf{r})$. The subscript "0" in $\langle \cdots \rangle_0$ indicates a configurational average to be evaluated in the unstrained state. Later, we will evaluate these expressions for ideal fcc and bcc lattices. In the conventional "Voigt notation" the four indices (range 1–3) are replaced by two indices (range 1–6). In this notation one denotes elastic moduli of cubic crystals and of the model with central interactions: $C_{11} \equiv G_{xx,xx}$, $C_{12} \equiv G_{xx,yy}$, and $C_{44} \equiv G_{xy,xy}$. The conventional symmetrization according to $C_{44} \equiv (G_{yx,yx} + G_{yx,xy} + G_{xy,yx} + G_{xy,xy})/4$ is not essential in this case. In this work, the axes x,y,z correspond to the directions [100], [010], [001] in the cubic crystal, i.e., to the deformation direction, its gradient direction, and the direction normal to the shear deformation plane, respectively. In systems with cubic symmetry, spatial anisotropy is reflected by the existence of a minimum and a maximum of the shear modulus. The modulus C_{44} is associated with a displacement in the [100] direction and a (010) shear plane in a cubic crystal. This modulus stands for a maximum resistance the system with fcc or bcc structure can offer to shear. The same systems, with a displacement applied along the [1$\bar{1}$0] direction and the (111) shear plane of the crystal, have minimum shear modulus associated with the modulus $\tilde{C}_{44} = (C_{11} - C_{12})/2$. For an isotropic system, C_{44} equals the orientationally averaged shear modulus G. As a component of the elastic modulus tensor, the shear modulus can be written as a sum of a Born-Green (usually positive) and a fluctuation (usually negative) contribution, $G = G^{\mathrm{BG}} + G^{\mathrm{flct}}$. The Born-Green contribution is written as a linear combination of the extremal contributions to the shear modulus, precisely,

$$G^{\mathrm{BG}} \equiv \frac{3C_{44} + 2\tilde{C}_{44}}{5}. \quad (8)$$

The fluctuation contribution to the average shear modulus becomes

$$VG^{\mathrm{flct}} = -\frac{\beta}{10}[6\langle \Phi_{xy}^2\rangle_0 + \langle (\Phi_{xx} - \Phi_{yy})^2\rangle_0]. \quad (9)$$

The response to a volume changing deformation of an isotropic solid can be inferred from the (isothermal) bulk modulus or compression modulus $B \equiv n(\partial p^{\mathrm{iso,pot}}/\partial n)_T$,

where $n = N/V$ is number density. The Born-Green components of the bulk and shear moduli are related in cubic crystals [34,35] via a modified Cauchy relation valid for the embedded-atom method of the form (1) through

$$B^{\mathrm{BG}} = \frac{5}{3}G^{\mathrm{BG}} + 2\,p^{\mathrm{pot}} + \frac{1}{9V}\left\langle \sum_i \left.\frac{\partial^2 \mathcal{F}}{\partial \rho^2}\right|_i \left(\sum_{j \neq i} r^{ij}\left.\frac{\partial w}{\partial r}\right|_{ij}\right)^2 \right\rangle_0. \quad (10)$$

The fluctuation contribution to the bulk modulus is

$$VB^{\mathrm{flct}} = -\frac{\beta}{9}[\langle \Phi_{\mu\mu}\Phi_{\mu\mu}\rangle_0 - \langle \Phi_{\mu\mu}\rangle_0^2], \quad (11)$$

and the total bulk modulus is $B = B^{\mathrm{BG}} + B^{\mathrm{flct}}$.

III. THE "GEAM" MODEL POTENTIALS

For the binary potential function $\mathcal{U}$ we use a radially symmetric short-ranged attractive (SHRAT) potential [36,37]:

$$\mathcal{U}(r) = \phi_0 r_0^{-4}[3(r_{\mathrm{cut}} - r)^4 - 4(r_{\mathrm{cut}} - r_{\mathrm{min}})(r_{\mathrm{cut}} - r)^3], \quad (12)$$

for $r \leq r_{\mathrm{cut}}$, and $\mathcal{U}(r) = 0$ otherwise, with an energy scale ϕ_0, a length scale r_0, an interaction range r_{min}, and a cutoff radius r_{cut}. The well depth of the two-particle (binary interaction) potential $\mathcal{U}$ is $-\mathcal{U}(r_{\mathrm{min}}) = \phi_0 r_0^{-4}(r_{\mathrm{cut}} - r_{\mathrm{min}})^4$. This format of the potential has been recently used as the effective two-particle interaction in the embedded-atom model metal [38–40], and to model thermophysical properties of fluids and solids [36]. The SHRAT potential has a finite value at $r = 0$, i.e., $\mathcal{U}(0) = \phi_0 r_0^{-4} r_{\mathrm{cut}}^3(4r_{\mathrm{min}} - r_{\mathrm{cut}})$. For temperatures below $0.1\phi_0/k_B$—due to the Boltzmann factor $\exp[-\mathcal{U}(0)/k_B T]$—the fraction of particles that reach zero distance is smaller than 10^{-51} for the choice $r_{\mathrm{cut}} = 1.6\,r_0$, $r_{\mathrm{min}} = 2^{1/6} r_0$. We use the normalized Lucy's weight function in the definition of the embedding density for reasons discussed in Ref. [38], i.e.,

$$w(r) = w_0\left(1 + 3\frac{r}{r_{\mathrm{cut}}}\right)\left(1 - \frac{r}{r_{\mathrm{cut}}}\right)^3, \quad (13)$$

for $r \leq r_{\mathrm{cut}}$, and $w = 0$ otherwise, with a prefactor obtained by normalizing the weight function, $w_0 = w(0) = 105/(16\pi r_{\mathrm{cut}}^3)$. The embedding potential in polynomial form is

$$\mathcal{F}(\rho) = \phi_0 \sum_{k=2,4,\ldots} F_k[(\rho - \rho_{\mathrm{des}})^k - (w_0 - \rho_{\mathrm{des}})^k]r_0^{3k}, \quad (14)$$

where ρ_{des} is the desired embedding number density and F_k are embedding strengths, being part of the model. Odd terms in the sum are excluded since their contribution would be always repulsive in nature, the linear term ($k = 1$) could be adsorbed in a modified pair potential $\mathcal{U}$. The desired density in this model equals roughly, $\rho_{\mathrm{des}} = r_0^{-3}$, the embedding density and particle number density $n \equiv N/V = r_0^{-3}$. Polynomial

TABLE I. The values of constitutive properties and their ratios for Cu, Ni, Ag, Au, Fe, and the model metal GEAM (ρ_{des}, F_2 are equal to unity and all other parameters are zero). The top values are experimental data from Refs. [44–47], and the two lower values are calculated for input parameters in the first four columns. The model parameters for the metals are obtained by linear optimization of ratios of constitutive properties using experimental data.

Metal	F_2	F_4	r_{cut}	$\dfrac{r_{min}}{2^{1/6}}$	n	E_{coh}	B	G	$\dfrac{nE_{coh}}{B}$	$\dfrac{E_{v1}}{E_{coh}}$	$\dfrac{G}{B}$	A
Cu					85.9 nm^{-3}	3.50 eV	142 GPa	59.3 GPa	0.339	0.366	0.418	3.19
(fcc)	0.42	0.	1.010	1.00	0.997	0.419	2.889	1.158	0.145	0.897	0.401	3.35
	0.42	8.5	1.010	1.00	0.997	0.972	2.909	1.158	0.333	0.412	0.398	3.35
Ni					84.6 nm^{-3}	4.45 eV	183 GPa	94.3 GPa	0.329	0.360	0.513	2.45
(fcc)	0.2	0.	1.017	1.02	0.957	0.366	2.408	1.202	0.145	1.034	0.499	2.95
	0.2	6.5	1.017	1.02	0.957	0.839	2.468	1.203	0.325	0.838	0.487	2.96
Ag					58.0 nm^{-3}	2.95 eV	101 GPa	33.5 GPa	0.271	0.373	0.331	2.88
(fcc)	0.7	0.	1.006	1.00	0.994	0.486	3.609	1.214	0.134	0.793	0.336	2.85
	0.7	8.	1.006	1.00	0.994	0.982	3.621	1.214	0.270	0.415	0.335	2.85
Au					58.1 nm^{-3}	3.81 eV	174 GPa	30.7 GPa	0.204	0.236	0.177	2.85
(fcc)	1.3	0.	0.988	0.94	1.052	0.281	4.890	0.842	0.125	0.514	0.172	2.92
	1.3	10.2	0.988	0.94	1.052	1.083	5.562	0.841	0.204	0.295	0.151	2.83
Fe					84.6 nm^{-3}	4.29 eV	169 GPa	86.8 GPa	0.344	0.417	0.515	2.70
(bcc)	0.2	0.	1.17	1.08	0.868	0.417	1.572	0.772	0.252	1.091	0.491	2.97
	0.2	1.1	1.17	1.08	0.868	0.417	1.667	0.768	0.342	0.724	0.491	2.97
GEAM					72.0 nm^{-3}	1.91 eV	179 GPa	52.7 GPa				
(fcc)	1.0	0.	1.00	1.00	0.993	0.552	4.442	1.309	0.123	0.718	0.295	2.34

format of embedding functional is computationally less expensive than standard logarithmic form [20–22]. Also, the ratio between cohesive energy E_{coh} (or energy per particle) and B can be systematically changed without influence on values of other constitutive properties of the system, see Table I. In the following section (Sec. III A) a property of polynomial format, to give simple analytical expressions for many constitutive properties, will be used to explain origins of well-known properties of embedded-atom potential [22].

We investigate a generic embedded-atom model metal with a minimum of the binary potential located at the distance $r = r_{min} = 2^{1/6} r_0 \approx 1.12 r_0$ as for the Lennard-Jones potential, with a cutoff distance $r_{cut} = 1.6 r_0$, and $F_2 = 1$, and $F_k = 0$ for $k > 2$. The hereby specified metal will be denoted as GEAM. For GEAM, the well depth of the two-particle potential $\mathcal{U}$ is therefore $-\mathcal{U}(r_{min}) \approx 0.05 \phi_0$. Model parameters for Cu, Ni, Ag, Au, Fe, and the GEAM model metal are given in Table I; parameters for the real metals are obtained by linear optimization using experimental data (ratios of the constitutive properties) also given in the table.

A. Basic properties

The energy per particle can be calculated from Eq. (1) for particles, which occupy ideal lattice sites. The resulting curves are displayed in Fig. 1 for GEAM with ($F_2 = 1$) and also without ($F_2 = 0$) the embedding contribution. The dependence of energy per particle from density is presented, and the dashed curves show results for particles placed on bcc lattice sites. The fcc and hcp structures are energetically equivalent for $n^{1/3} r_{cut} < 1.83$. For densities close to $n = r_0^{-1/3}$ (or $n = 1$ in reduced units, cf. Sec. III B) the mini-

mum energy is lower in fcc solids. In order to describe the influence of model parameters on some constitutive properties of ideal fcc and bcc structures we will consider a state point with vanishing (total) isotropic pressure and fix the binary potential well depth to the above GEAM value. The shape of the binary potential is controlled by changing the values r_{min} and r_{cut}. The size of r_{cut} changes the strength of contributions to the embedding density. Smaller r_{cut} means smaller contribution of neighbors, $\Sigma_{i \neq j} w(r^{ij})$, in Eq. (2). The corresponding parameter in other embedded-atom models, cf. Refs. [22,23], is the nearest neighbor equilibrium distance.
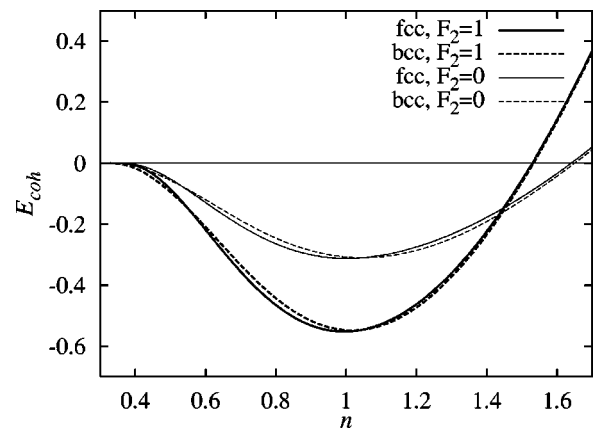

FIG. 1. Cohesive energy or energy per particle vs density (both in LJ units) at $r_{cut} = 1.6 r_0$, $r_{min} = 2^{1/6} r_0$ (generic embedded-atom model GEAM) for ideal fcc and bcc lattices with ($F_2 = 1$) and also without ($F_2 = 0$) the embedding functional.
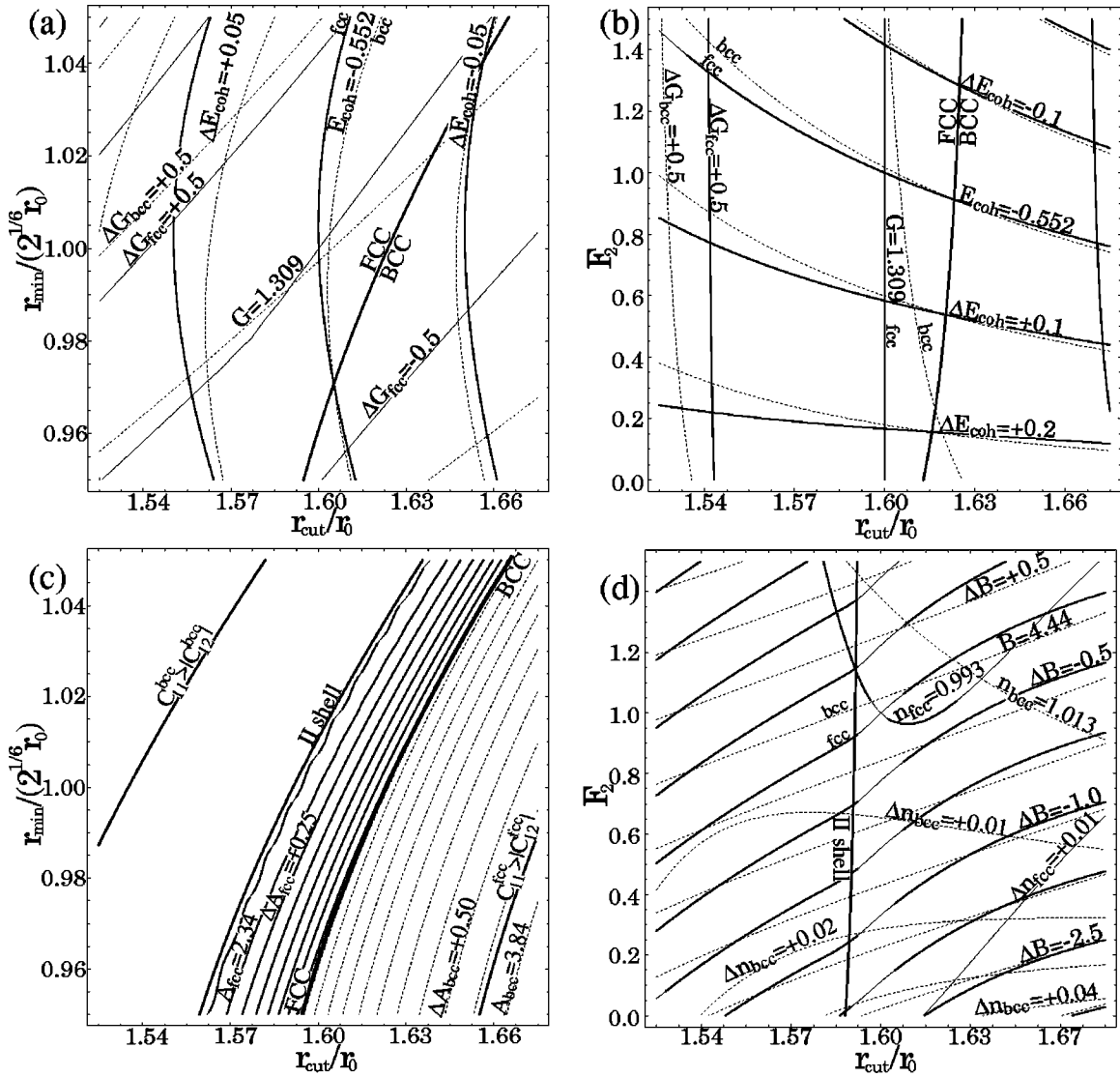
FIG. 2. Cohesive energy E_{coh}, shear G and bulk B moduli, anisotropy ratio A, and density n for the case of vanishing pressure tensor. All quantities are in standard LJ units. Values for fcc (solid curves) and bcc (dashed curves) structure are presented. (a) Effect of cutoff radius r_{cut}, position of the potential minimum r_{min} for $F_2=1$ (GEAM). (b) Effect of cutoff radius r_{cut} and embedding strength F_2 for $r_{min}=2^{1/6}r_0$ (GEAM). (c) Effect of r_{cut}, r_{min} ($F_2=1$) on the anisotropy ratio A. Areas (bold line) where fcc and bcc structures are energetically favored are also shown. For cubic structures one has $A=2$ if interactions with the first nearest neighbor shell only are present; "II shell" denotes the separation line. The line $C_{11}>|C_{12}|$ separates the regimes where bcc and fcc structures are mechanically unstable. (d) Effect of r_{cut}, F_2 (for $r_{min}=2^{1/6}r_0$) on the bulk modulus B and zero-pressure density n.

In the following, elastic coefficients, pressure tensor, and related quantities are evaluated from the expressions given in the preceding section in the limit of low temperatures, where particles occupy ideal lattice sites.

The cohesive energy $E_{coh} \equiv E/N$, or energy per particle, depends strongly on the embedding part of the model potential, see Figs. 2(a) and 2(b) for a quantitative analysis. The main contribution of the two-particle interaction to E_{coh} stems form the first neighbors. At zero pressure, the first neighbors are near the minimum of the binary potential; the resulting density depends only on the position of the minimum of the potential [Fig. 2(d)]. Since the well depth of the two-particle potential is held constant, the cohesive energy does not depend on the position of the potential minimum.

The vacancy formation energy E_{1v} is the minimum energy needed to move an atom from the bulk onto the surface of the crystal [20,22]. In order to perform a systematic analysis pf E_{1v} parameter dependence, relaxation of structure around vacancy is not considered. The dominant contribution in EAM to the unrelaxed vacancy formation energy stems from the binary interaction potential. The unrelaxed vacancy formation energy depends weakly on the embedding part of the potential and the position of the cutoff radius, cf. Table I. It depends indirectly—through zero-pressure density—on the position of the potential minimum. Compared to other constitutive properties of EAM metals, the unrelaxed vacancy formation energy changes slowly with a change of all model parameters. Other ground state defect energies of the model

metal, e.g., the surface formation energy, can be also calculated from Eq. (1).

Recent studies, Refs. [41,42], indicate that there is no straightforward comparison between vacancy formation and surface formation energies calculated with EAM and experimental data. Difference between electronic structure at a surface level and in bulk is not considered by EAM, thus EAM should give in case of metal with high electronic density (Pt,Pd) noticeably lower vacancy formation energies from experiment.

The elastic coefficients—bulk modulus B, (average) shear modulus G, C_{44}, and the Cauchy pressure $\tilde{C}_{44} = (C_{11} - C_{12})/2$—depend on the second derivative of the free energy for a nearest neighbor model, cf. Eq. (6). The second-order term [$k=2$, Eq. (14)] in the embedding functional is most important for the values of the elasticity coefficients which include response of material on volume changes (B, C_{11}, C_{12}) since the embedding density is usually very close to the desired embedding density, see Fig. 2(d). Shear moduli C_{44} and $\tilde{C}_{44}$ in cubic crystals include only response to volume conserving shear deformation that do not change embedding density and consequently contribution of embedding functional to free energy. For this reason shear moduli depend only on two-body interaction parameters $(r_{\text{cut}}, r_{\text{min}})$, see Figs. 2(a) and 2(b). The same conclusion can be obtained from symmetry analysis of Eq. (6) for cubic crystals. This enables us to fit experimental values for the shear moduli G and bulk moduli B independently by varying strength of F_2 term. Other order terms of embedding functional may be considered to obtain an improved quantitative agreement between model behaviors and experimentally observed behaviors, in particular with respect to the ratios between elastic coefficients and the cohesive energy, cf. Table I. Due to Eq. (10), the difference between bulk and shear modulus is approximately

$$(3B - 5G) \approx \frac{nF_2}{3} \left(\sum_{j \neq i} r^{ij} \frac{\partial w}{\partial r} \bigg|_{ij} \right)^2 \qquad (15)$$

near the zero-pressure density in an ideal cubic crystal. The ratio $G/B \lesssim 3/5$ decreases with increasing second-order term in the embedding functional.

The so-called "anisotropy ratio" $A = C_{44}/\tilde{C}_{44}$ of a cubic material is the ratio of the extremal values of the shear modulus, maximum C_{44} and minimum Cauchy pressure $\tilde{C}_{44}$. It depends on the shape of weighting function and the two-particle potential. It does not depend on the embedding strength (F_2). The anisotropy ratio is $A=2$ in cubic crystals, when only interactions with nearest neighbors are present, according to Cauchy relations. In bcc structure the Cauchy pressure falls with increasing cutoff radius and the anisotropy ratio rises. If the Cauchy pressure becomes negative, the system is mechanically unstable for zero applied stress, see Fig. 2(c). For the mechanical stability analysis in case of nonzero stresses one should use modified stability criteria, see Ref. [43]. Even when disregarding the higher order terms, the embedded-atom potential (14) predicts well the anisotropy ratios of both fcc and bcc metals. Higher order

terms ($F_4, F_6, \dots$) can be considered to obtain a quantitatively improved description (Table I) predominantly concerning the cohesive energy. Other constitutive properties stay mostly unchanged upon considering these higher order terms.

B. Reference values

To compare nonequilibrium molecular dynamics (NEMD) simulation results with experimental data, we relate constitutive properties of our model with experimental data for real metals in Table I. The last four columns of this table give the characteristic ratios of constitutive properties for four fcc metals (Cu,Ni,Ag,Au) and one bcc metal Fe, together with the same ratios for corresponding model metals obtained by linear optimization of model parameters; values for GEAM are also listed. The reference values for dimensionless model quantities Q_{dimless} can be computed from experimental (top number) and calculated values listed in middle section of Table I. The determined model parameters and reference values are not unique in the sense that it is possible to find similar sets which would as well resemble the properties of real materials. Concerning reference values used to translate between dimensionless simulation quantities and experimental values, we should discuss them shortly. Any measurable quantity Q with a dimension $[Q]$ specified in SI units kg, m, and s is made dimensionless by a reference quantity

$$Q_{\text{ref}} = m^{\alpha + \gamma/2} r_0^{\beta + \gamma} \phi_0^{-\gamma/2} \quad \text{for } [Q] = \text{kg}^\alpha \text{m}^\beta \text{s}^\gamma, \quad (16)$$

such that $Q = Q_{\text{dimless}} Q_{\text{ref}}$; quantities m, r_0, and ϕ_0 provide the scales via the interaction potential (12) and the equations of motion. The reference values for length r, number density n, energy $k_B T$ (and defect energies), temperature T, time t, shear rate $\dot{\gamma}$, pressure P, and the elastic moduli in terms of the simulation parameters are therefore $r_{\text{ref}} = r_0$, $n_{\text{ref}} = r_0^{-3}$, $e_{\text{b,ref}} = \phi_0 = k_B T_{\text{ref}}$, $t_{\text{ref}} = r_0 (m/e_{\text{b,ref}})^{1/2}$, $\dot{\gamma}_{\text{ref}} = t_{\text{ref}}^{-1}$, and $P_{\text{ref}} = \phi_0 r_0^{-3} = n_{\text{ref}} e_{\text{b,ref}}$. For Cu, e.g., one obtains reference values $\phi_0 = 3.61$ eV and $P_{\text{ref}} \equiv 38$ GPa, $r_0 = 2.26$ Å, and $n_{\text{ref}} = 86.2$ nm^{-3} from Table I. Atomic mass of copper is $m_{\text{Cu}} = 1.06 \times 10^{-25}$ kg and the reference time is estimated as $t_{\text{ref}} = 0.97 \times 10^{-13}$ s. By choosing $T_{\text{ref}} = \phi_0/k_B = 40$ kK, $P_{\text{ref}} = 40$ GPa one obtains $\phi_0 = 3.45$ eV, $n_{\text{ref}} = 72.5$ nm^{-3}, and $r_0 = 2.4$ Å for GEAM.

The predicted values of the vacancy formation energy, elastic anisotropy, and the bulk modulus are within the expected ranges for fcc and bcc metals. Since both density and vacancy formation energy depend strongly on the position of the potential minimum, there is no unique way to choose model parameters such that both density and vacancy formation energy precisely match values for a given real metal, cf. Table I and Figs. 2(a) and 2(b) for possible choices.

C. Implementation of the model

The equations of motion in the conducted NEMD simulation are integrated by a velocity-Verlet algorithm. A cubic simulation box with constant volume and Lees-Edwards periodic boundary conditions are used to simulate shear defor-

mation. Details about the implementation can be found in Refs. [39,48–51]. The force acting on particle i, directly obtained from Eq. (1), reads

$$\mathbf{F}_i = -\sum_{j \neq i} \left[\left. \frac{\partial \mathcal{U}}{\partial \mathbf{r}} \right|_{ij} + \left(\left. \frac{\partial \mathcal{F}(\rho)}{\partial \rho} \right|_i + \left. \frac{\partial \mathcal{F}(\rho)}{\partial \rho} \right|_j \right) \left. \frac{\partial w}{\partial \mathbf{r}} \right|_{ij} \right]. \quad (17)$$

A suitable integration time step is $\Delta t / t_{\text{ref}} = 0.01$ for the chosen range of temperatures and densities. The temperature is kept constant by rescaling the magnitudes of the peculiar particle velocities which corresponds to a Gaussian constraint of constant kinetic energy in the limit $\Delta t \to 0$.

For the case of a model metal under steady shear deformation (or flow), a relative motion of periodic images in the flow (x) direction is performed, with a shear gradient in the y direction. The flow simulation introduces the shear rate $\dot{\gamma}$, given by $\dot{\gamma} = \partial v_x / \partial y$, as a further independent variable. While a linear flow profile is observed at moderate rates, at higher shear rates and during the transition towards a steady state, parts of the system move as blocks. To allow simulations of pluglike flow, in this paper is used a "profile unbiased thermostat," which calculates the mean peculiar velocities self-consistently. The details of this temperature control method are given elsewhere, see Refs. [52,53]. Alternatively, shear flow can also be generated by modifying the equations of motion with a Sllod algorithm [54,55].

The values of the shear stress components are obtained by extracting their averages once the system has reached the stationary state. This corresponds to the statistical average typically over a period $\Delta t / t_{\text{ref}} = 800$ in system of 2000 particles, the configurations are sampled after every 10 time units. The temperature was increased stepwise every $\Delta t / t_{\text{ref}} = 2000$. The results for pressure tensor components for a number of parameters are compared with data extracted from NEMD simulations of larger systems ($N = 43\,000$) and runs $\Delta t / t_{\text{ref}} = 4000$ to test convergence to steady state. The stick-slip motion is observed only in intermediate state and it is not observed after first 1000 time units of the simulation. System size effects on total energy, pressure tensor components, and their fluctuations are not observed. Yield stress and frequency of defects formed in steady state shear regime depend through energy needed to form a defect on the system size, see Ref. [56]. Thus, it is important to use a large number of particles ($N > 5000$) to obtain relevant information about value of yield stress and stationary state structure of system.

For our systems, the total simulated physical time will be of the order of $10^{-10} - 10^{-9}$ s which is smaller than the minimum "lifetime" of an asperity. The minimum lifetime, in a process of solid friction, is estimated by the size of an average asperity (10 μm) divided by a high velocity, e.g., 100 m/s in case of thread breaking [57–59]. Concerning both length and time scales, the simulated systems may represent only a fragment of an asperity. For this reason, the properties of the system such as overall density, pressure, and temperature are taken to be constant within the simulation cell. The simple model metal is explicitly determined by the set of
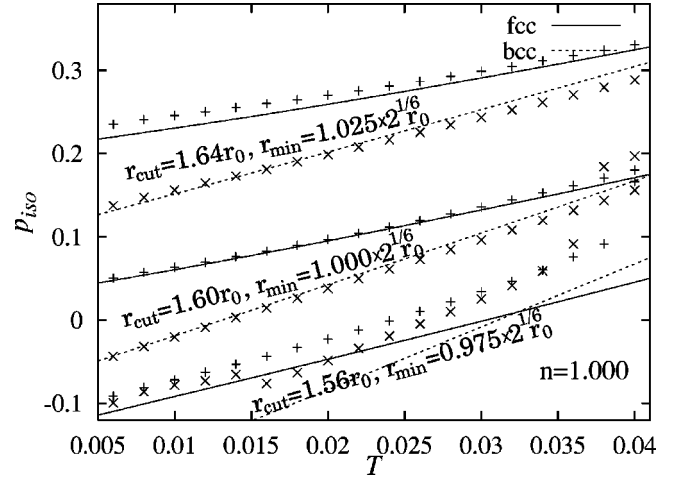

FIG. 3. Pressure as function of temperature (in standard LJ units) for different model parameters, cutoff r_{min} and minimum of the potential r_{min}. Molecular dynamics (MD) simulation results for p^{iso} are denoted with + (bcc configuration) and × (fcc). The curves represent the approximate expression for the pressure, Eqs. (18) and (19). Global density in the system is $n = 1.00$.

model potentials and solved without approximations with computational effort of order N.

IV. EQUILIBRIUM PROPERTIES

When material is subjected to deformation or an increase of temperature, it responds with changes of its free energy and pressure. At low temperatures the particles are near to their positions in an ideal crystal. The isotropic "cold" pressure $p_{\text{cold}}(n)$ is calculated by inserting distances of nearest neighbors (for an ideal lattice) into Eq. (3). A modification of the known expression for the cold pressure has been recently used to model the isotropic pressure at finite temperatures for the case of the SHRAT potential used here, see Ref. [36]. The adapted formula for the pressure takes into account that with increasing temperature particles approach each other more closely, and reads

$$p_{\text{solid}}(n,T) = n k_B T + \tfrac{1}{2} \{ p_{\text{cold}}[n + s_F(n,T)] \\ + p_{\text{cold}}[n - s_F(n,T)] \}. \quad (18)$$

We observe that the factor $s_F(n,T)$ depends on the strength of the embedding functional $\mathcal{F}$ (here only F_2 is considered) and also on the type of crystal structure as follows:

$$s_F^{\text{fcc}}(n,T) \approx \sqrt{(5.25 - 1.25 F_2) \frac{k_B T}{e_2}},$$

$$s_F^{\text{bcc}}(n,T) \approx \sqrt{(4.5 + 0.5 F_2) \frac{k_B T}{e_2}}. \quad (19)$$

We have $s_F^{\text{fcc}}(n,0) = s_F^{\text{bcc}}(n,0) = 0$ and $e_2 = \partial^2 E_{\text{coh}} / \partial n^2$. Equation (19) improves the corresponding expression given in Ref. [36]. Though one could discuss further corrections to the expression for $s_F(n,T)$, the proposed Eq. (19) shows good agreement with simulation results as demonstrated by

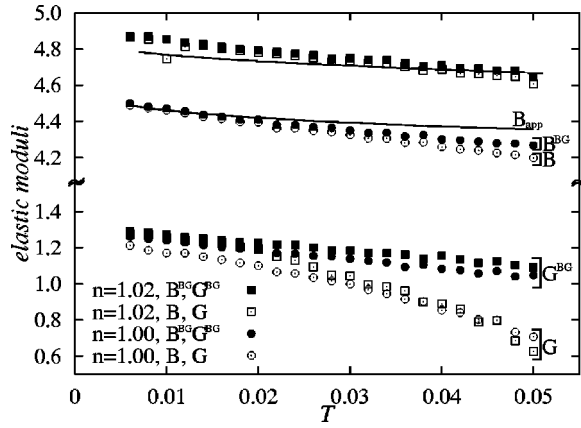FIG. 4. Shear modulus (G), bulk modulus (B), and their Born-Green contributions vs temperature for densities $n = 1.00, 1.02$ for GEAM in dimensionless LJ units, obtained via nonequilibrium molecular dynamics (NEMD). The curve for bulk modulus (B_{app}) is calculated inserting the approximate expression for pressure, Eqs. (18) and (19), into the definition of bulk modulus.

Fig. 3. This figure presents equilibrium molecular dynamics (MD) results for the heating of the EAM metal (at $n = 1.00$) for different model parameters. The temperature is increased stepwise between $T = 0.006$ and 0.04 ($\Delta T = 0.002$ each 1000 time units). In Fig. 3, MD results for p^{iso} are denoted by symbols, and lines stem from the analysis based on the above expressions (18) and (19). The system can withstand tension due to internal attraction, when the pressure is negative. This is a consequence of the presence of boundary conditions at fixed volume. For the large negative pressures (model parameters: $r_{min} = 0.975 \times 2^{1/6}$, $r_{cut} = 1.56$, $F_2 = 1$) holes in the system are created, and the system does not reach a stable state within the simulation time. For the
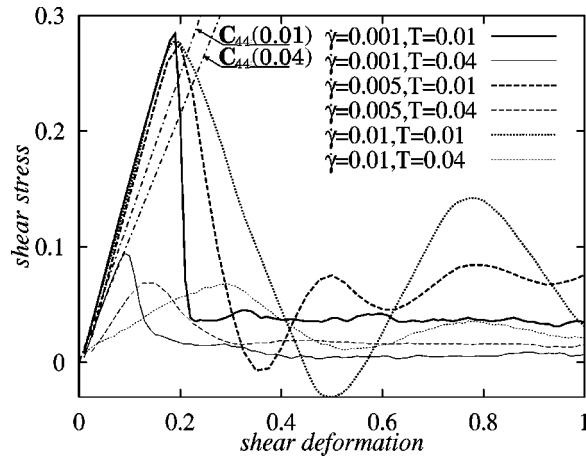

FIG. 5. Shear stress as function of deformation for three shear rates $\dot{\gamma} = 0.001$, 0.005, and 0.01 at two temperatures $T = 0.01$ (thicker curve) and $T = 0.04$ (thinner curve) of GEAM, obtained via NEMD. The starting configuration is the ideal fcc structure at density $n = 1.00$ with $N = 43\,000$ particles. The shear started at $t = 0$. Shear direction is the [100] direction in crystal, and shear plane coincides with the (010) crystal plane. The coefficient C_{44} is obtained via MD simulation. All quantities are given in LJ units.

same system, melting is observed near the temperature $T = 0.035$.

The isothermal bulk modulus and shear modulus determine the elastic properties of an isotropic solid. Using the approximate expression for the isotropic pressure [Eqs. (18) and (19)], an approximate expression for the bulk modulus is obtained directly. It is shown in Fig. 4 for a range of temperatures and densities where the system is solid. The elastic moduli decrease with increasing temperature. At higher temperatures the fluctuation contribution to the shear modulus is of the same order of magnitude as the Born-Green contribution. In the molten state the shear modulus vanishes.

V. MECHANICAL PROPERTIES DURING STEADY SHEAR

A. Plastic yield

Representative results of the NEMD simulation concerning elastic response and plastic yielding of the solid GEAM are presented in Fig. 5. The system responds with growing shear stress ($-P_{xy}$) to an increasing shear deformation $\gamma = \dot{\gamma} t$ (constant shear rate $\dot{\gamma}$) switched on at $t = 0$. In this figure, shear stress is plotted as function of shear deformation for an initially prepared fcc GEAM metal at temperatures $T = 0.01, 0.04$ and three different shear rates $\dot{\gamma} = 0.001, 0.005$, and 0.01 (reduced units). The axes x, y, z correspond to the directions [100], [010], [001] in the initial crystal structure. It is seen that the yield deformation does not depend on the shear rate for $T = 0.01$. This may be expected in view of Lindemann's criterion which says that a crystal will melt when the amplitude of vibration (x_0) of atoms exceeds about one-tenth of the lattice constants. The smaller values of the yield deformation at high temperature $T = 0.04$ and $\dot{\gamma} = 0.001$ can be also explained by this criterion. If we assume a harmonically oscillating motion of atoms, we obtain the relation $kT = f x_0^2 / 2$ between temperature and the amplitude of vibrations, where f stands for an effective spring coefficient between an atom and its neighborhood. The coefficient f can be related to elastic moduli, see Ref. [60], and it falls with temperature. High temperatures and a small spring coefficient result in a large amplitude of oscillations and a small yield deformation.

The plastic behavior following the yield point, however, depends on shear rate. At high rates (and high temperatures) defects are formed immediately after a yield stress is reached. This results in a slowdown of the relaxation of accumulated stress at high shear rates. Under these conditions, soon after the yield point has been reached (here at $\gamma = 0.1$), shear-induced melting is observed. During this intermediate state (inhomogeneous melting), a layer of liquid metal is formed between two blocks of the solid metal, and the blocks are moving at constant speed, see upper left cross section in Fig. 10. Actually, the periodic simulation cell contains 34 layers of particles and an effective shear rate at the position of the layer is $\sim 34\dot{\gamma}$—just at startup of flow. For this reason, for systems at temperatures near the melting point ($T = 0.04$) and at high shear rates $\dot{\gamma} = 0.005, 0.01$ the system partially melts soon after the shear commenced. In

TABLE II. Coefficients in approximate expressions for shear stress, $-p_{xy}=a_T T+c$, in Figs. 6 and 7 for different values of model parameters r_{cut}, r_{min}, and F_2 (all other parameters are zero).

$\dfrac{r_{min}}{2^{1/6}}$	$\dfrac{r_{cut}}{1.6}$	F_2	$\dot{\gamma}$	a_T	c
1.	1.	0.	0.001	$-0.34(6)$	0.037(1)
1.	1.	0.5	0.001	$-0.47(6)$	0.039(2)
1.	1.	1.	0.001	$-0.44(5)$	0.045(1)
1.	1.	1.	0.010	$-0.37(5)$	0.040(1)
1.025	0.95	1.	0.001	$-0.5(2)$	0.092(5)
1.025	1.05	1.	0.001	$-0.64(7)$	0.055(2)

Ref. [61], a similar behavior is observed during sliding of a tetrahedral tip (Cu) over a Ni substrate via simulation. The stick-slip motion is observed, with abrupt structural transition of the tip layer closest to the substrate between two slips in which Cu (110) surface transformed into (111) surface to match (111) surface structure of Ni substrate. Two comparisons with inhomogeneous melting in our system can be made.

(i) We also observe regions in intermediate shear regime (before stationary state structure is formed, Fig. 5), where motion is converted to the strain energy. A part of strain energy is spent on the structure change (melting) of the structure between the blocks and the rest is dissipated throughout the system.

(ii) The structure of fluid at interface tends to match the interface surface structure [61,62]. The observed melting is a result of two opposed mechanisms, blocks have fcc (100) surface structure but the system tends to form fcc (111) structure in this plane (see Sec. VI).

The measured yield stress decreases considerably with temperature, since particles at comparatively high tempera-
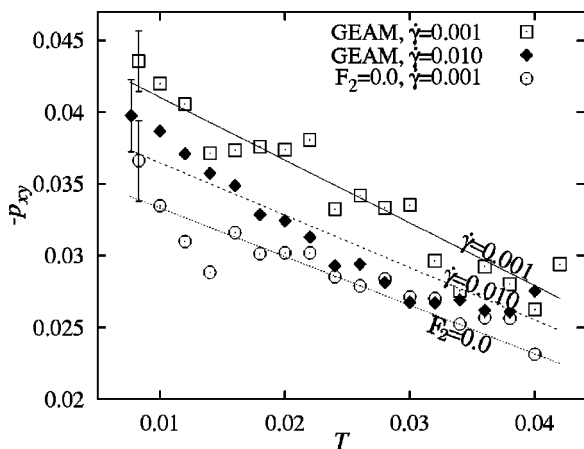

FIG. 6. Shear stress vs temperature. Symbols denote averages from the NEMD simulation of GEAM with different densities for two shear rates $\dot{\gamma}=0.001,0.01$ ($F_2=1$) and for $F_2=0$ ($\dot{\gamma}=0.001$). All quantities are expressed in LJ units. Curves are obtained by linear regression analysis of the simulation results. Estimated error ranges (standard deviation) have similar size for all data points, for this reason they are plotted only at $T/T_{ref}=0.08$.
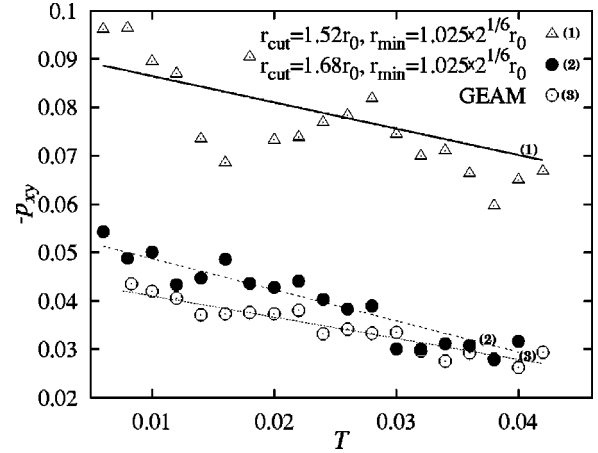

FIG. 7. Shear stress as function of temperature (in standard LJ units) for different model parameters, minimum r_{min} and cutoff radius of the potential r_{cut}. Symbols denote averages from the NEMD simulation at shear rates $\dot{\gamma}=0.001$. Curves are obtained by linear regression analysis of the simulation results.

tures can cross the potential barrier and enter the next potential minimum faster.

B. Rheological properties for stationary shear flow

For a planar Couette flow the symmetric traceless pressure tensor (which equals the negative stress tensor) has only three independent components $p_{+,-,0}$, a shear pressure $p_+ \equiv P_{xy}$ or shear stress $-P_{xy}$, and two normal pressure differences: $p_- \equiv (P_{xx}-P_{yy})/2$, $p_0 \equiv [2P_{zz}-(P_{xx}+P_{yy})]/4$. We calculate (via NEMD) the pressure tensor over the range of temperatures $T=0.008,\dots,0.06$, for densities $n=0.98,\dots,1.08$, and for two shear rates $\dot{\gamma}=0.001,0.01$. These simulations are performed with 1000, 2000, and 43 000 particles.

In order to discuss the relationship between shear stress and temperature for two shear rates we test a simple linear relationship between them, where the coefficients are obtained via regression. Within statistical errors and for the range of chosen densities, we did not detect an effect of density on the friction pressure. The resulting approximate expressions are given in Table II. The regression curves of shear stress ($-p_+$ or $-P_{xy}$) together with the simulation data are presented in Fig. 6. Data are plotted for two shear rates $\dot{\gamma}=0.001$ (solid curve), $\dot{\gamma}=0.010$ (dashed curve) and $\dot{\gamma}=0.001, F_0=0$ (dotted curve). The shear stress decreases with increasing temperature. This is so, because atoms have large kinetic energies and can move uncorrelated and far from their equilibrium positions as compared to atoms in a layer plane. For the same reason, the observed shear stress decreases with increasing shear rate. At a higher shear rate more defects are produced and the ordering of atoms into hexagonal layers is weakened, see the insets of Fig. 10. The embedding contribution reduces density fluctuations, making atoms more bounded into layer structure, thus shear stress decreases with decreasing influence of embedding contribution, cf. Table II and Fig. 6. The simulated values of the two normal pressure differences $p_{-,0}$ are found to both vanish
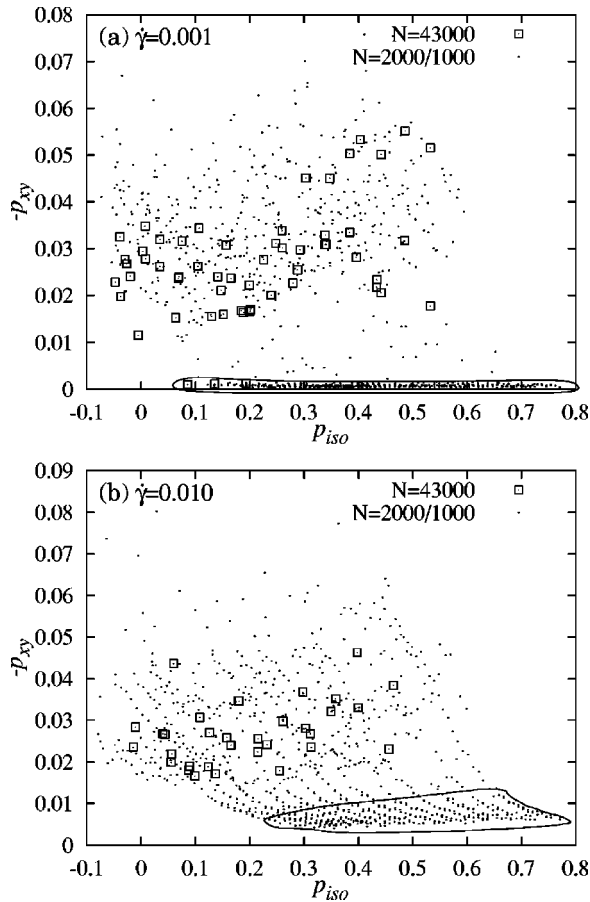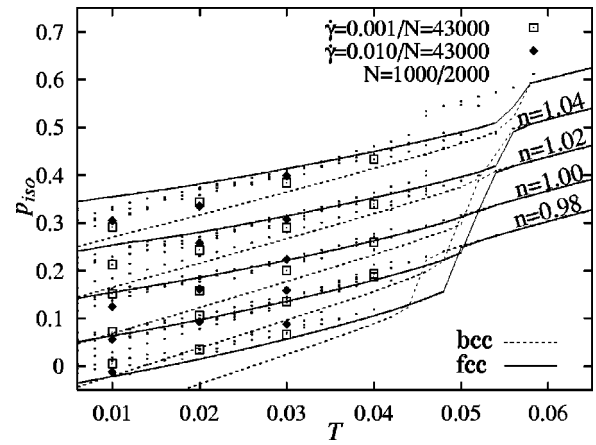
FIG. 9. Effect of temperature on the isotropic part of the pressure of the system under shear. Symbols indicate results from NEMD simulation of GEAM at different densities, number of particles, temperatures, and shear rates. The curve for isotropic pressure comes from the molecular dynamics simulations of melting for different densities for bcc and fcc structure (without shear). All quantities are given in standard LJ units.

FIG. 8. Shear stress $-p_{xy}$ vs the isotropic part of the pressure, for two shear rates: (a) $\dot{\gamma}=0.001$ and (b) $\dot{\gamma}=0.01$. Symbols indicate results from NEMD simulations of GEAM for different densities and temperatures. All quantities are given in LJ units. Data points where the system is molten are encircled with a line.

within the precision of our data. In Fig. 7, the data are presented for three systems: GEAM (with fcc ground state structure and shear moduli $G=1.31$), for model parameters $r_{min}=1.025\times2^{1/6}$, $r_{cut}=1.68$, $F_2=1$ (bcc, $G=1.33$) and $r_{min}=1.025\times2^{1/6}$, $r_{cut}=1.52$, $F_2=1$ (fcc, $G=2.39$). Since the shear stress and moduli have the same origin in shape of two-body interaction potential, the observed shear stress increases linearly with increase of the shear moduli. The dependencies of shear stress on temperature and shear rate are particularly important when the metal is subject to severe stresses or nonuniform heating, e.g., as result of thread breaking [57–59].

In a liquid metal, atoms are quite free to move and the system exhibits a comparable small resistance to the shear flow, cf. the enclosed points in Figs. 8(a) and 8(b). This means that if the model metal stays crystalline (during shear) it mostly reduces energy per particle rather than reducing resistance to shear. Thus, the observed reordering of the crystal structure under shear has little in common with the mechanism responsible for an ordering transition—accompanied by shear thinning—observed in fluids [63]. The present transition is similar to an ordering phenomenon observed experimentally and predicted theoretically for colloi-

dal crystals in solid state [65]. However, in colloidal crystals the shear stress rises at the melting transition [63–65]. The structure in a colloid is formed to reduce the resistance to shear. Only if the shear rate and the temperature are sufficiently low, the system can reduce the potential energy by forming periodic crystal structures. In metals the interaction between atoms is stronger than in colloids and the mechanism which tries to reduce the potential energy of the system is dominant. The data points in Fig. 8 stem from NEMD simulations at different densities, shear rates, and temperatures.

The equilibrium and nonequilibrium values for the isotropic pressure are shown in Fig. 9 as function of temperature T and density n. The symbols mark the computed pressure for the system under shear. The curves represent the evolution of the isotropic pressure during melting of a bcc system (dashed curve) and a fcc system (solid curve) without shear. The increase of pressure at high temperatures indicates the onset of a shear-induced melting [66]. For the high densities ($n=1.02,1.04$), the observed structure in the system is mainly of bcc type, resulting in an isotropic pressure smaller than the one for the corresponding fcc structure.

In case of dry solid friction between two blocks made of the same material, the load is related to the isotropic pressure inside the interface (asperity). Except in case of polished surfaces, all asperities will be in state of incipient flow, see Ref. [14]. The simulation cell can be regarded as containing a typical part of such an interface. The typical value of the isotropic pressure should be therefore estimated from the penetration hardness, which is defined as the ratio between load N and contact area A at the onset of plastic flow. For most metals, the penetration hardness lies in the range 0.005–0.025 [reduced Lennard-Jones (LJ) units] [14,15]. From simulation data in Fig. 9 it is visible that with and also without shear one can consider the penetration hardness as a good estimate for the average isotropic pressure within an
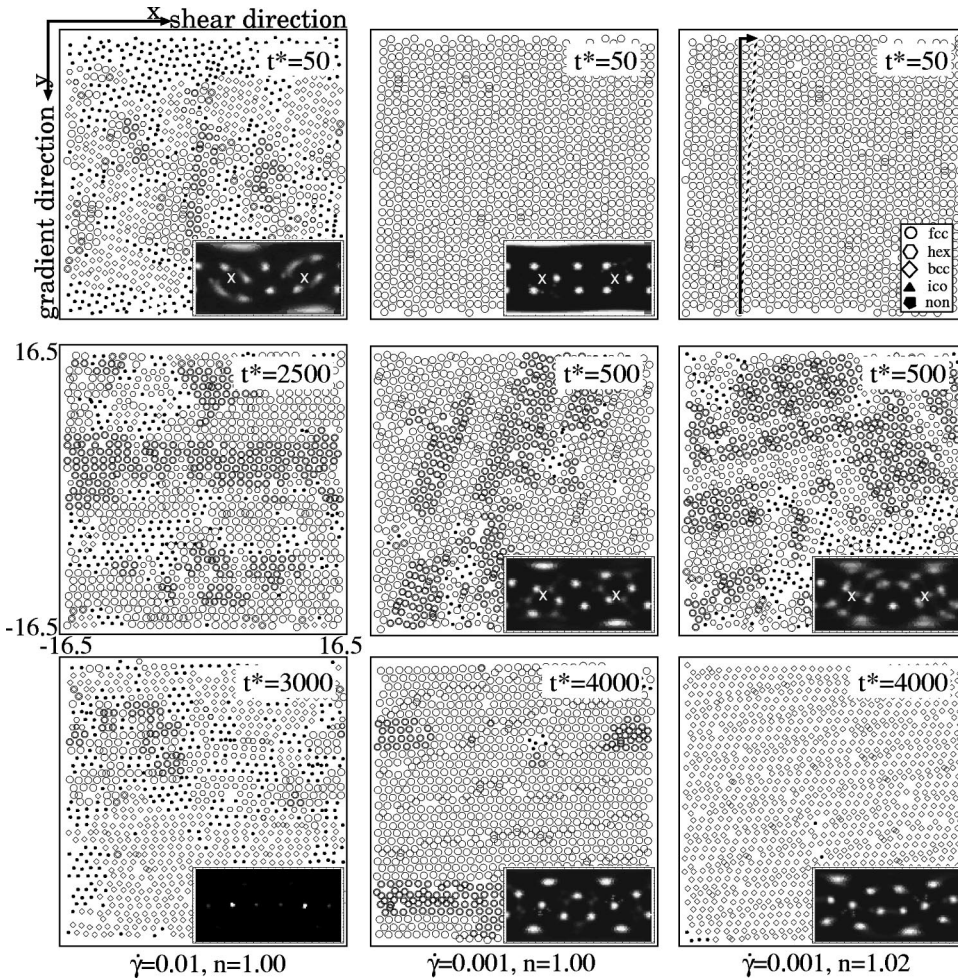
FIG. 10. Snapshots (via NEMD) visualizing the evolution of the GEAM crystal subject to steady shear deformation at different times. All quantities are expressed in LJ units. The number of particles is $N = 43\,000$, temperature $T = 0.02$. Each slice is one length unit wide. Snapshots for two different shear rates $\dot{\gamma} = 0.001, 0.01$ and densities $n = 1.00, 1.02$ are presented. The type of local structure is indicated. The start configuration is the ideal fcc structure, shearing started at $t = 0$. The directions of shear and gradient directions are indicated in upper right picture. The insets contain the angular distribution of closest neighbors, where the representation is such that the shear direction projects at points denoted with $\times$ and the plane normal to flow gradient direction projects on a line (of length 2π) connecting the $\times$ points.

asperity. The friction coefficient is defined as the ratio between shear stress (integrated over the volume of an asperity) and the load. Under the assumption for sufficiently high loads, e.g., large surfaces of asperities, that the isotropic pressure and the shear stress are homogeneous inside the asperity we obtain via NEMD a "macroscopic" friction coefficient μ in the range between 0.2 and 3, defined as $\mu \equiv -p_{xy}/p^{\mathrm{iso}}$. These values are comparable to the ones for real materials. With the available mesoscale methods, such as smooth particle hydrodynamics, which allow to simulate a surface containing several asperities it would be possible to obtain improved values for the analog to the experimentally measured, macroscopic, friction coefficient. Such an investigation is outside the scope of the present paper.

The shear stress does not change as much as the isotropic pressure does during variation of temperature and density. Even at large isotropic pressures above $p^{\mathrm{iso}} = 0.4$, which is realized in shock waves and impact experiments, the shear stress stays near its value at zero pressure. Strings of the data points, visible in the Fig. 8(b), can be understood resulting from partial melting of the system at high temperatures. Partial melting is observed at the (larger) shear rate $\dot{\gamma} = 0.010$, at temperatures below $T = 0.04$. Shear-induced melting is observed at temperatures above $T = 0.04$, see Fig. 12. We will further comment on this figure in the following section.

VI. STRUCTURAL CHANGES DURING STEADY SHEAR

In the preceding section we demonstrated that shear stress rises before reaching the yield stress for a system subject to shear deformation. After reaching this stress, atoms tend to move into the next potential minima while the system relaxes, as is also reflected by oscillations in Fig. 5. If the shear continues, significant structural changes appear in the system. Shear-induced structural local (re)ordering is followed by changes in the streaming profile and by a buildup of long-range order.

Figure 10 shows a time series for a subsystem of a cubic cell with $N = 44\,000$ particles undergoing shear at two different densities $n = 1$ and $n = 1.02$ and small and intermediate rates $\dot{\gamma} = 0.001$ and $\dot{\gamma} = 0.01$, respectively. The snapshots (including structure analysis) show a cut of width $\Delta r = 1$ of the full system, and the direction of shear is depicted in the top right snapshot. Another quantitative analysis of the evolution of the crystal morphology for the same system with time is presented in Fig. 11. We used a common neighbor analysis method [24] based on planar graphs to extract information about structure from the NEMD data. The method is based on a suitable definition for "neighboring atoms." The list of the neighbors is used as an input for a pattern recognition which resolves fcc, bcc, hcp, as well as icosahedral structure (ico). The ico structure preferably occurs in amorphous sol-
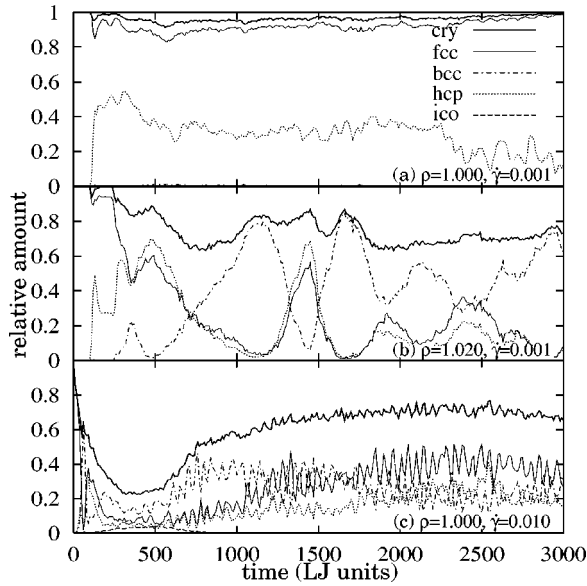
FIG. 11. Transient behavior of the relative volumes occupied by fcc, bcc, and hcp structures, together with the volume occupied by the amorphous icosahedral structure (ico), obtained via NEMD, for GEAM at two shear rates $\dot{\gamma}=0.001,0.01$ and densities $n = 1.00,1.02$. The bold curve (cry) represents relative volume occupied by the three crystalline structures together. Domains with different crystal structures can overlap, thereby the total amount of crystallinity (cry) is not a sum of relative volumes occupied by fcc, bcc, and hcp structures. Time is given in standard LJ units and the number of particles is $N=43\,000$, temperature $T=0.02$. Starting configuration is the ideal fcc structure, shearing started at $t=0$.

ids. The ratio between all atoms which are found to belong to a structure (central atom plus its neighbors, no double counting) and total number of atoms in the system is taken as measure of the amount of certain crystal structure. For our model all three crystal structures are observed. At high shear rates ($\dot{\gamma}=0.01$), the icosahedral structure is observed in an intermediate state, see Fig. 11.

At the shear rate $\dot{\gamma}=0.001$, after the yield stress had been reached, a sudden increase in the amount of hcp structure is observed from Fig. 11, the crystal planes shear oblique to the shear direction and form a defect. The defect is visible in the cross section shown in this figure for $t=500$ as the area where both hcp and fcc structures are present. The generated defect blocks flow and induces a further increasing shear stress. Particles gain kinetic energy by randomly moving away from the defect. As a result, the system melts locally. This causes the appearance of gradual rearranged areas around the defects in the system. To make this more visible we also provide the angular distribution of directions to next neighbors in the insets in Fig. 10. The shear direction is marked with two crosses ($\times$) in the insets, and the plane normal to flow gradient projects on a line (not drawn) connecting the crosses. During this structural transition two-dimensional densely packed layers are formed where the shear direction is in parallel with the nearest neighbor direction at $t=3000$ in Fig. 10, visible as strings of particles. In the stationary state the distance which the particles cross be-
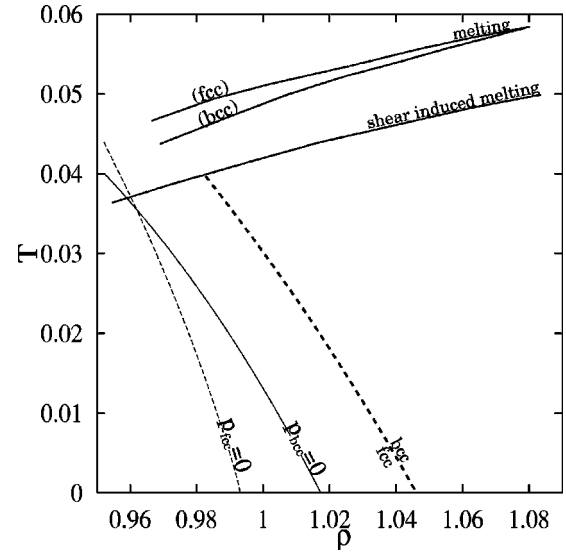

FIG. 12. Structural phase diagram of GEAM in the temperature-density plane for two shear rates $\dot{\gamma}=0.001,0.01$. The bold dashed curve separates the densities and temperatures where at low shear rates ($\dot{\gamma}=0.001$) bcc or fcc structure is dominant. The area where system is mechanically unstable due to internal attraction is estimated by inserting Eqs. (18) in condition $p^{\mathrm{iso}}=0$. Upper three (solid) curves show melting temperatures with and without shear.

tween two minima is the smallest possible in the system. This reduces the probability for creating new defects. The densely packed layers are stacked along the gradient direction to maximize the distances between particles as they shear past each other and reduce resistance to shear. For the fcc structure the most densely packed planes correspond to the (111) plane and the shear direction to the $[1\bar{1}0]$ direction. The corresponding plane and direction in a bcc structure are (110) and $[111]$, respectively.

Shear deformation inherently generates defects since atoms can move oblique to the shear direction to reach some close-by energetically preferred states and therefore prevent the shear stress from relaxing. The formation and evolution of the defects is observed and discussed. Even when stationary flow is reached, shear in direction oblique to shear flow is observed resulting in deviations from stationary shear flow profile.

The boundary condition imposes a further constraint on the newly formed crystal structure. Crystal planes tend to contain a multiple of unit crystal cells between the boundaries of the system. This results in a small deviation between densely packed planes and plane normal to the flow gradient, which may increase the probability for the appearance of defects. We studied several system sizes to make sure that the presented results are not artificially driven by finite size effects.

For $\dot{\gamma}=0.01$ the structure of the system changes between randomly close packed (fcc and hcp) and bcc; see Fig. 11. The total amount of crystallinity is almost constant. We ob-

serve that the bcc structure is produced by a volume conserving Bain transformation [67] of parts of the fcc structure. This process is reversible. The reason for such a behavior of the system is that the system cannot globally adjust itself to accommodate deformation. Therefore, density fluctuations arise. The fcc and hcp structures have the same energy per particle in the limit of low temperatures and always occur together as randomly close packed structures. Though one could expect to observe an identical amount of fcc and hcp structures, in our simulations the fcc structure shows up to be dominant. The explanation should be that the hcp structure allows shearing only in a single plane and that it is less resistant to defects, as compared to fcc. At higher densities and temperatures the bcc structure becomes dominant.

Nonequilibrium phase diagram

The condition $p^{iso}=0$ is used in Eq. (18) to estimate the area of mechanical instability due to internal attraction of GEAM under shear in the nonequilibrium phase diagram, cf. Fig. 12. Cracks—several crystal constants wide—are observed for small densities and low temperatures. The constant volume condition prevents their growth. The upper three (solid) curves show melting temperatures with and without shear. Shear-induced melting is observed at temperatures above $T=0.04$. In equilibrium, the system melts at temperatures above $T=0.045$. In this diagram the bold dashed curve separates the densities and temperatures where at low shear rates ($\dot{\gamma}=0.001$) bcc or fcc structures are dominant, cf. Fig. 11. In the limit of low temperatures the preferred structure can be calculated directly from Eq. (1). With increasing temperature the bcc structure becomes dominant at densities where the fcc structure dominates at low temperatures. The crystal structure formed under the influence of shear exhibits a large shear stress compared to the one in the liquid metal. It appears that the crystal structure is formed to reduce the free energy of the system. The shear deformation in this picture cancels the influence of the boundary conditions. This fcc-bcc transition happens at pressures which are so high that they should usually be inaccessible for unconfined metals.

At high temperatures the bcc structure is observed at densities, where the fcc structure dominates at lower temperatures. This should be an important finding. Such a phase transition in solid part of the nonequilibrium phase diagram was assumed to exist in colloidal crystals [64,65]. *Ab initio* calculations of solid phases in transition metals [67–69] suggest that the observed high temperature bcc structure might be stabilized by a lattice vibrational entropy contribution to the free energy. Molecular dynamics simulations were recently used [70] to determine the vibrational entropy.

VII. CONCLUSIONS

The GEAM model potential introduced in Sec. III was used to study plastic deformation, yield, and steady shear of metals. We analyzed its mechanical behavior and the transient local crystal structure. We showed that structural information can be related to the pressure tensor in order to understand the influence of different conditions (density, shear rate, temperature) on the evolution of the components of the pressure tensor after onset of shear. We offered expressions for the pressure tensor, the elastic modulus tensor (Born-Green and fluctuation contributions), and average elasticity moduli for particles interacting with the embedded-atom model potential. We applied these expressions to fcc, bcc crystal structures and liquid model metals (they could be applied as well to other crystal structures such as simple cubic, hexagonal close packed, or diamond cubic). The low degree polynomial format of the potential yields a simple dependency of the ground state constitutive properties on model parameters. In Table I we illustrate that the main constitutive properties of real metals are reproduced with a few model parameters. Thermomechanical properties of our model have been calculated using MD simulation. An expression for the cold isotropic pressure was adapted to fit the simulation results for a wide range of model parameters at different temperatures and densities. In addition, the average of the bulk modulus has been determined from MD and compared to its counterpart calculated from an approximate expression for the pressure. The analytic formula for the isotropic pressure, Eq. (18), can be used as a closure relation (constitutive relation) in the mesoscale simulation techniques [28–31] discussed in the Introduction. As demonstrated in Sec. VI, the isotropic pressure of the system is determined by the equilibrium pressure of the dominant structure when subjected to steady shear. This finding extends the application of the formula, Eq. (18), to other systems under steady shear deformation.

We explored the influence of temperature on the values for the yield deformation and the relaxation behavior of the accumulated stress. The generation of defects, and the local melting of the system, prevents stick-slip motion at low shear, as observed earlier for the pure SHRAT fluid, cf. Ref. [36]. The plastic yield and friction stress have been analyzed within asperities on the nanometer scale. Local densities, temperatures, and shear rates inside the asperity are input parameters for the NEMD simulations. The friction process itself is seen here as a combined effect of processes on a microscale (size of asperities) and a nanoscale. The mesoscale methods [28–31] are expected to overcome the gap between the micrometer scale and the nanometer scale. These methods need a phenomenological model that describes the behavior of the pressure tensor components under deformation. The results presented in this paper may serve as motivation for new models that incorporate structural changes and their effect on the pressure tensor in a metal subject to shear deformation and flow.

[1] J.P. Hirth, Acta Mater. **48**, 93 (2000); J.P. Hirth and J. Lothe, *Theory of Dislocations*, 2nd ed. (Wiley, New York, 1982).

[2] Z. Shen, R.H. Wagoner, and W.A.T. Clark, Acta Metall. **36**, 3231 (1988).

[3] H.M. Zbib and T.D. de la Rubia, Int. J. Plast. **18**, 1133 (2002).

[4] J. Schiøtz, T. Vegge, F.D. Di Tolla, and K.W. Jacobsen, Phys. Rev. B **60**, 11 971 (1999).

[5] F.F. Abraham, R. Walkup, H. Gao, M. Duchaineau, T.D. de la Rubia, and M. Seager, Proc. Natl. Acad. Sci. U.S.A. **99**, 5783 (2002).

[6] C.M. Mate, in *Handbook of Micro/Nano Tribology*, edited by B. Bhushan (CRC Press, Boca Raton, 1995), p. 167.

[7] *Nanoscience: Friction and Rheology on the Nanometer Scale*, edited by E. Meyer, T. Gyalog, R. M. Overney, and K. Fransfeld (World Scientific, Singapore, 1998).

[8] M.R. Sørensen, K.W. Jacobsen, and P. Stoltze, Phys. Rev. B **53**, 2101 (1996).

[9] O.M. Braun and M. Peyrard, Phys. Rev. E **63**, 046110 (2001).

[10] M.H. Müser and M.O. Robbins, Phys. Rev. B **61**, 2335 (2000); M.H. Müser, L. Wenning, and M.O. Robbins, Phys. Rev. Lett. **86**, 1295 (2001).

[11] Z.N. Farhat, Wear **250**, 401 (2001).

[12] J.P. Hirth and D.A. Rigney, in *Dislocations in Solids*, edited by F.R. Nabarro (North-Holland, Amsterdam, 1983), Vol. 6, p. 10.

[13] D.R. Wheeler and D.H. Buckley, Wear **33**, 65 (1975).

[14] B.N.J. Persson, *Sliding Friction*, 2nd ed. (Springer, Berlin, 2002).

[15] F.P. Bowden and D. Tabor, *The Friction and Lubrication of Solids*, 2nd ed. (Clarendon Press, Oxford, 1954).

[16] B.N.J. Persson, J. Chem. Phys. **115**, 3840 (2001); B.N.J. Persson, F. Bucher, and B. Chiaia, Phys. Rev. B **65**, 184106 (2002).

[17] V.D. Scott and T. Wilman, Proc. R. Soc., Math. Physic. Eng. Sci. **247**, 353 (1958).

[18] J.-P. Poirier, *Creep of Crystals* (Cambridge University Press, Cambridge, 1985).

[19] K. Kadau, T.C. Germann, P.S. Lomdahl, and B.L. Holian, Science **296**, 1681 (2002).

[20] B.L. Holian, A.F. Voter, N.J. Wagner, R.J. Ravelo, S.P. Chen, W.G. Hoover, C.G. Hoover, J.E. Hammerberg, and T.D. Dontje, Phys. Rev. A **43**, 2655 (1991).

[21] M.S. Daw and M.I. Baskes, Phys. Rev. Lett. **50**, 1285 (1983); Phys. Rev. B **29**, 6443 (1984).

[22] R.A. Johnson, Phys. Rev. B **37**, 3924 (1988); **37**, 6121 (1988); **39**, 12 554 (1989).

[23] F.J. Cherne, M.I. Baskes, and P.A. Deymier, Phys. Rev. B **65**, 024209 (2001).

[24] I. Stankovic, M. Kröger, and S. Hess, Comput. Phys. Commun. **145**, 371 (2002).

[25] A. Böhmer and T. Klimpel, Wear **253**, 150 (2002).

[26] F. Bucher, K. Knothe, and A. Theiler, Wear **253**, 204 (2002).

[27] M. Ertz and K. Knothe, Wear **253**, 498 (2002).

[28] J.J. Monaghan, Annu. Rev. Astron. Astrophys. **30**, 543 (1992).

[29] L.D. Libersky, A.G. Petschek, T.C. Carney, J.R. Hipp, and F.A. Allahdadi, J. Comput. Phys. **109**, 67 (1993).

[30] M. Ellero, S. Hess, and M. Kröger, J. Non-Newtonian Fluid Mech. **105**, 35 (2002).

[31] B.I.M. ten Bosch, J. Non-Newtonian Fluid Mech. **83**, 231 (1999).

[32] S. Hess, M. Kröger, and W.G. Hoover, Physica A **239**, 449 (1997).

[33] M. Born, J. Chem. Phys. **7**, 591 (1939); Proc. Cambridge Philos. Soc. **36**, 160 (1940); H.S. Green, *The Molecular Theory of Fluids* (North-Holland, Amsterdam, 1952); M.S. Green, J. Chem. Phys. **22**, 398 (1954).

[34] L.A. Shuvalov, A.A. Urusovskaya, I.S. Zheludev, A.V. Zalessky, S.A. Semiletov, B.N. Grechushnikov, I.G. Chistyakov, and S.A. Pikin, *Modern Crystallography IV* (Springer, Heidelberg, 1998), pp. 51–85.

[35] R.A. Johnson, in *Many-Atom Interactions in Solids*, Springer Proceedings in Physics Vol. 48 (Springer, Berlin, 1990), pp. 85–102.

[36] S. Hess and M. Kröger, Phys. Rev. E **64**, 011201 (2001).

[37] S. Hess and M. Kröger, Techn. Mech. **22**, 79 (2002).

[38] W.G. Hoover and S. Hess, Physica A **267**, 98 (1999).

[39] M. Kröger and S. Hess, Z. Angew. Math. Mech. **90**, Suppl. 1, 48 (2000).

[40] M. Kröger, I. Stankovic, and S. Hess, Multiscale Model. Simul. **1**, 25 (2003).

[41] K. Carling, G. Wahnström, T.R. Mattsson, A.E. Mattsson, N. Sandberg, and G. Grimvall, Phys. Rev. Lett. **85**, 3862 (2000).

[42] T.R. Mattsson and A.E. Mattsson, Phys. Rev. B **66**, 214110 (2002).

[43] J. Wang, S. Yip, S.R. Phillpot, and D. Wolf, Phys. Rev. Lett. **71**, 4182 (1993).

[44] Y.R. Wang and D.B. Boercker, J. Appl. Phys. **78**, 122 (1995).

[45] M.S. Daw, Phys. Rev. B **39**, 7441 (1989).

[46] K. Fuchs, Proc. R. Soc. London, Ser. A **153**, 622 (1936).

[47] *American Institute of Physics Handbook*, 3rd ed., edited by Dwight E. Gray (McGraw-Hill, New York, 1972).

[48] M.P. Allen and D.J. Tildesley, *Computer Simulation of Liquids* (Clarendon, Oxford, 1987).

[49] A.W. Lees and S.F. Edwards, J. Phys. Chem. **5**, 1921 (1972).

[50] M. Kröger, W. Loose, and S. Hess, J. Rheol. **37**, 1057 (1993).

[51] M. Kröger, C. Luap, and R. Muller, Macromolecules **30**, 526 (1997).

[52] S. Hess and W. Loose, Physica A **162**, 138 (1989).

[53] W.G. Hoover, Annu. Rev. Phys. Chem. **34**, 103 (2983); D.J. Evans and G.P. Morriss, Comput. Phys. Rep. **1**, 287 (1984); D.J. Evans and W.G. Hoover, Annu. Rev. Fluid Mech. **18**, 243 (1986).

[54] W.G. Hoover, Physica A **194**, 450 (1993).

[55] D.J. Evans and G.P. Morriss, *Statistical Mechanics of Nonequilibrium Liquids* (Academic Press, London, 1990).

[56] M.F. Horstemeyer, M.I. Baskes, and S.J. Plimpton, Acta Mater. **49**, 4363 (2001).

[57] J.F. Archard, Wear **2**, 438 (1958).

[58] G.J. Moyar and D.H. Stone, Wear **144**, 117 (1991).

[59] M.R. Johnson, R.E. Welch, and K.S. Yeung, J. Eng. Ind. **99**, 18 (1977).

[60] D. Tabor, *Gases, Liquids and Solids*, 3rd ed. (Cambridge University Press, Cambridge, 1993).

[61] A. Buldum and S. Ciraci, Phys. Rev. B **55**, 12 892 (1997).

[62] P.A. Thompson and M.O. Robbins, Phys. Rev. A **41**, 6830 (1990).

[63] W. Loose and S. Hess, Rheol. Acta **28**, 91 (1989).

[64] B.J. Ackerson, J.B. Hayter, N.A. Clark, and L. Cotter, J. Chem. Phys. **84**, 2344 (1986); B.J. Ackerson and P.N. Pusey, Phys.

Rev. Lett. **61**, 1033 (1988); B.J. Ackerson, J. Rheol. **34**, 553 (1990).

[65] M.J. Stevens, M.O. Robbins, and J.F. Belak, Phys. Rev. Lett. **66**, 3004 (1991); M.J. Stevens and M.O. Robbins, Phys. Rev. E **48**, 3778 (1993).

[66] M.I. Baskes, Phys. Rev. Lett. **83**, 2592 (1999).

[67] P.J. Craievich, M. Weinert, J.M. Sanchez, and R. E Watson, Phys. Rev. Lett. **72**, 3076 (1994).

[68] A. Chang, C. Colinet, M. Hillert, Z. Moser, J.M. Sanchez, N. Saunders, R. E Watson, and A. Kussmaul, CALPHAD: Comput. Coupling Phase Diagrams Thermochem. **19**, 481 (1995).

[69] P.J. Craievich, J.M. Sanchez, R. E Watson, and M. Weinert, Phys. Rev. B **55**, 787 (1997).

[70] U. Pinsook, Phys. Rev. B **66**, 024109 (2002).